ACS Sustainable Chemistry & Engineering

pubs.acs.org/journal/ascecg

Research Article

Calculation of Resonance Raman Spectra and Excited State Properties for Blue Copper Protein Model Complexes

Umut Ozuguzel, Adelia J. A. Aquino,* Reed Nieman, Shelley D. Minteer, and Carol Korzeniewski*

Cite This: *ACS Sustainable Chem. Eng.* 2022, 10, 14614−14623

Read Online

ACCESS | Metrics & More | Article Recommendations | Supporting Information

ABSTRACT: Laccase enzymes have been investigated for their potential as eco-friendly biofuel cell cathode catalysts. In these applications, electrons transfer from the electrode directly to the so-called Type 1 (T1) redox site within the enzyme. Over the years, resonance Raman (RR) spectroscopy has been utilized to probe the nature of ligand interactions with the Cu^{2+} center at the T1 site of the resting, oxidized form of laccases and related blue copper proteins. Spectral interpretation has been guided by parallel studies of small molecule T1 site mimics. Reported herein are results of time-dependent density functional theory (TDDFT) calculations performed on a series of experimentally well-studied T1 site mimics based on Cu^{2+} thiolate complexes stabilized by either a tridentate tris(pyrazolyl)hydroborate ligand or a bidentate β-diketiminate ligand. Vertical excitation energies were computed for the first 10 doublet states of each complex. The electronic absorption and RR spectra derived show excellent agreement with the experiment. RR spectra were dominated by a strong Cu−S stretching transition near 400 cm^{-1}, which is sensitive to molecular conformation within the thiolate ligand. The results provide a foundation to build from in advancing models of laccase catalytic active sites in support of sustainable technologies.

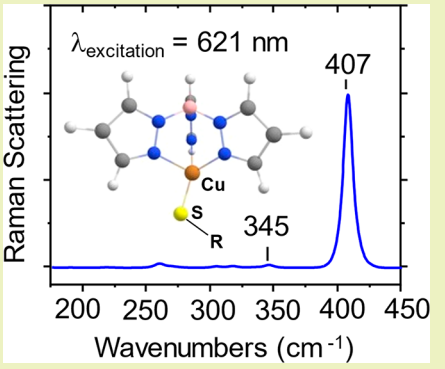

KEYWORDS: *Laccase, TDDFT, charge transfer, absorption, and Raman spectra*

INTRODUCTION

In the pursuit of practical renewable energy systems, fuel cells play a central role with many gains in recent years being led by improvements in the performance of electrocatalyst materials.[1−5] Among the approaches to lowering electrocatalytic reaction barriers are bioinspired strategies that leverage understanding of structure at enzyme active sites.[4−6] The ability to engineer pathways for facile electron transfer between enzyme catalytic centers and bulk electrode materials has opened opportunities in recent years to advance platforms for sustainable electrochemically driven processes, such as ambient temperature NH_3 synthesis from N_2,[7−9] CO_2 capture and conversion to useful chemical feedstocks,[10,11] and electricity production from biofuel cells.[5,6]

A fundamental challenge in the progression of fuel cells is the need to develop catalysts that improve cathode efficiency.[1−3,6] Efforts in this area have focused on materials for reducing O_2 to H_2O, given the convenience of O_2 as a reactant source and innocuous nature of the H_2O product. For biofuel cells, promising advances have been made in the development of cathodes based on laccases, enzymes able to transform O_2 directly to H_2O with the stability, activity, and versatility needed for practical fuel cell operation.[6,12−16] Within the class of Cu-containing redox proteins, laccases have been shown to undergo direct electron transfer with metal electrodes.[6,12,13,15,17,18] The enzymes contain four Cu atoms arranged into two catalytic centers.[6,17,19] The Type 1 (T1) center contains a single ligated Cu atom that facilitates substrate oxidation. Electrons shuttle from the T1 site through the protein to a trinuclear cluster, composed of one Type 2 (T2) Cu site and one binuclear Type 3 (T3) Cu site, where the transformation of O_2 to H_2O occurs.[6,17,19]

As a step toward the advancement of *in situ* spectroscopic methods in electrochemistry, we recently applied confocal Raman microscopy for quantitation of protein and plasticizing components within biocatalytic membranes.[20] Using laccase membranes as a model, vibrational spectral features of ligands surrounding the catalytic T1 center were detectible as a consequence of resonant enhancement effects, opening the possibility to interrogate the enzyme active site of biocathodes under fuel cell reaction conditions. Over the years, the technique of resonance Raman (RR) spectroscopy has been a valuable probe of molecular and electronic structure in laccases and the related blue Cu proteins.[21−29] For excitation within the envelope of the strong electronic absorption transition peaked near 600 nm for species in their resting oxidized states,[19] three dominant RR vibrational bands

Received: August 10, 2022
Revised: October 13, 2022
Published: October 24, 2022

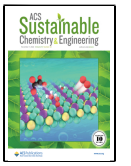

between 380 and 420 cm^{-1} have often been reported for laccase enzymes.[21,29,30] The electronic excitation near 600 nm has been assigned to $S(p\pi) \rightarrow Cu^{2+}(d_{x^2-y^2})$ charge transfer within the ligand bridge connecting the T1 site Cu atom and strongly coordinated cysteine group.[19,21] The RR band positions and intensities are sensitive to molecular structures near the T1 site and have been correlated to the T1 site S−Cu^{2+} bond strength and thermodynamic reduction potential.[21,27,30] Transition metal complexes that mimic the catalytic sites within blue copper proteins have been central to the development of mechanisms for enzymatic activity.[19,22,23,31] RR spectra of these mimics and enzyme mutants have revealed the significance of vibrational coupling in contributing to the strength of transitions through the 380 and 420 cm^{-1} regions in RR spectra of laccase enzymes, as well as the activation of charge transport between the T1 site and the trinuclear T2/T3 sites during O_2 reduction.[21,23,31]

Computational methods have been important to advancing understanding of laccase RR spectra. The Spiro group used classical vibrational force fields to explain trends in RR spectra of blue copper proteins and model T1 center compounds.[31] The synthetic models studied, based on Cu^{2+} thiolate complexes stabilized by the tris(pyrazolyl)hydroborate ligand system (Scheme 1), reproduce key structural and electronic

Scheme 1. Tris(pyrazolyl)hydroborate Cu^{2+} Thiolate Complexes Modeled, Where R = Triphenylmethyl, *tert*-Butyl, *sec*-Butyl, or Pentafluorophenyl, and R′ = H[a]

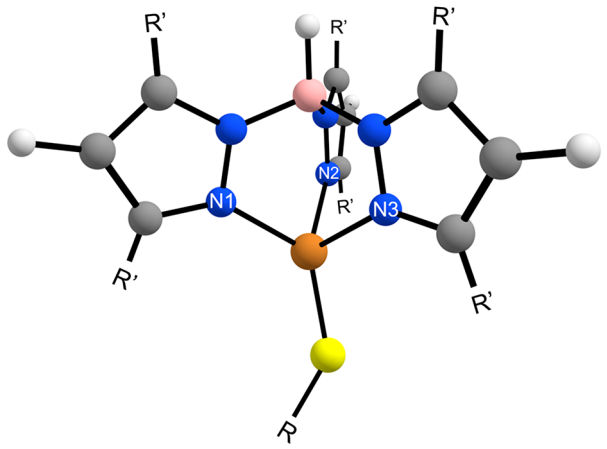

[a]In experimental studies discussed,[22,31] R′ = isopropyl. Color scheme: copper = orange, sulfur = yellow, carbon = dark gray, hydrogen = light gray, nitrogen = blue, boron = pink.

properties of the proteins.[32,33] Exploring structural variation within the thiolate ligand revealed subtle effects of coupled vibrational motion that affect the intensities of the RR bands for the complexes. Subsequently, Solomon and co-workers performed quantum chemical calculations that shed light on the electronic states accessed in the excitation of RR scattering for the class of Cu^{2+} T1 center mimics depicted in Scheme 1.[22,23]

Building from these theoretical chemical foundations, the work reported herein assesses the performances of modern quantum chemical methods in the development of laccase T1 site structural models to support *in situ* RR studies of laccase catalytic membranes. The ORCA program suite[34] was applied to evaluate electronic absorption and RR spectra of Scheme 1 complexes. The spectra obtained are in close agreement with the experiment and, combined with full results of the calculations, provide insights into the optically driven electronic and vibrational transitions responsible for features in measured spectra of the compounds. The study provides a framework for advancing models of laccase catalytic active sites and demonstrates the potential of modern quantum chemical methods to support the interpretation of measured electronic and vibrational spectra that provide insights needed to guide the development of sustainable technologies.

COMPUTATIONAL DETAILS

All calculations were performed with the ORCA program suite[34] (version 5.0). Density functional theory (DFT) was applied to carry out full ground state geometry optimizations. The Becke three-parameter Lee, Yang, and Parr (B3-LYP)[35] functional was used in combination with the resolution of identity[36] method allowing efficient calculation of the two-electron integrals. Unless otherwise stated, the def2-TZVP triple-ζ valence polarization basis set[37] was used. Normal coordinate vibrational frequency calculations were performed within the harmonic approximation taking the B3-LYP/SVP5[38] approach to confirm that each optimized structure is at an energy minimum. The smaller SVP basis set was used for this minimum energy confirmation. All studied compounds corresponded to a minimum energy in the ground state. The Cartesian coordinates of the optimized geometry (B3-LYP/def2-TZVP) can be found in Tables S18−S25 of the Supporting Information (SI).

The excited state calculations employed time-dependent density functional theory (TDDFT). Vertical excitation energies were computed for the first ten doublet states. Calculated UV−visible absorption spectra were processed with a custom Python script that performed the convolution of line spectra with Gaussian band shape (0.19 eV full width at half-maximum, fwhm, unless otherwise stated) functions. Resonance Raman spectral plots were generated within ORCA using the default Lorentzian function and 10 cm^{-1} fwhm spectral line width. Charge transfer (qCT)[39] was analyzed in terms of the transition density matrix and natural transition orbitals (NTOs)[40] using the TheoDore program.[39,41,42]

All calculations were carried out on isolated Scheme 1−3 compounds without the inclusion of environmental effects.

RESULTS AND DISCUSSION

Excited States and Oscillator Strengths. Table 1 shows vertical excitation energies, oscillator strengths, and qCT quantities for the 10 lowest excited states of the Scheme 1 compound that contains a triphenylmethyl thiolate ligand ($SCPh_3$). The $SCPh_3$ complex was the focus of early investigations, where the isopropyl groups in the synthesized compound (so-called "Complex 1")[22] were replaced by hydrogen atoms for efficiency in computational modeling.[22,31] Compilations similar to Table 1 for Scheme 1 and other compounds investigated in this work are included in the SI (Tables S1−S7). In each case, the charge transfer value was computed with reference to three fragments: the tris(pyrazolyl)hydroborate ligand (Fragment 1), the Cu atom (Fragment 2), and the thiolate ligand (Fragment 3). Note that the vertical excitations were also computed using the long-range ωB97X-D3 functional[43] as it is known that DFT using standard functionals does not describe well the charge transfer

https://doi.org/10.1021/acssuschemeng.2c04802
ACS Sustainable Chem. Eng. 2022, 10, 14614−14623

Scheme 2. Structures Showing Atom Numbering and Newman Projections Down the C−S Bond for Staggered (A, C, and D) and Eclipsed (B) Conformations of the Scheme 1 Compound Containing the *sec*-Butyl Thiolate Ligand Studied

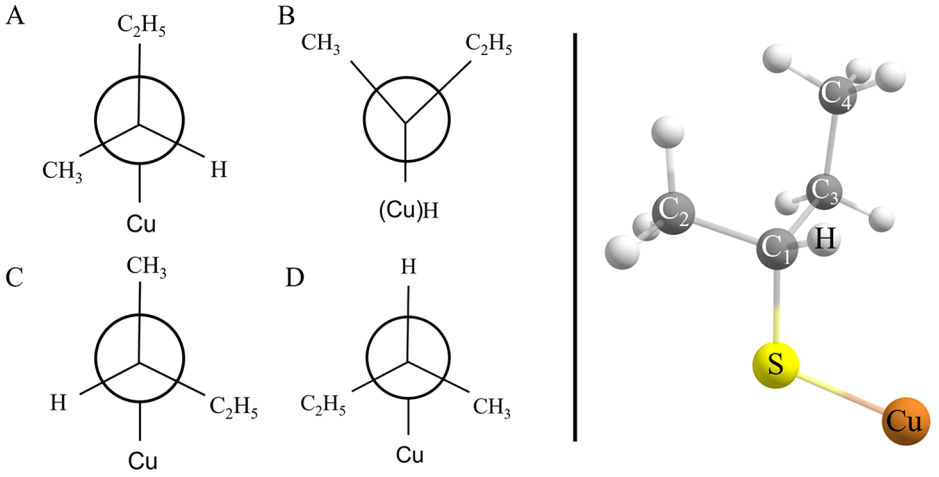

Scheme 3. Small Molecule ($L_2CuSCPh_3$) Mimic of the Fungal Laccase T1 Site[23,a]

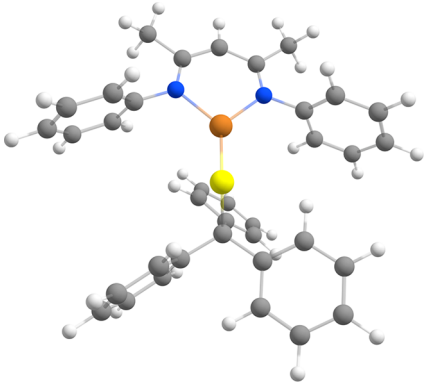

[a]See Scheme 1 legend for atom color scheme.

Table 1. Calculated B3-LYP/def2-TZVP Vertical Excitation Energies (Δ*E*), Oscillator Strengths (*f*), and Charge Transfer (qCT) Values of Scheme 1 Compounds Containing Triphenylmethyl Thiolate ($SCPh_3$)

Excited states	Δ*E*/eV[a] (nm)	*f*	qCT (*e*)	Δ*E*/eV[a,b] (nm)	*f*[b]
1 ^{2}A	0.711 (1744)	0.000	0.549		
2 ^{2}A	0.895 (1385)	0.001	0.576		
3 ^{2}A	1.446 (857)	0.016	0.578		
4 ^{2}A	1.527 (812)	0.000	0.565	1.342 (924)	0.009
5 ^{2}A	1.998 (621)	0.100	0.568	1.374 (903)	0.0033
6 ^{2}A	2.211 (561)	0.003	0.551	1.984 (645)	0.0713
7 ^{2}A	2.277 (545)	0.000	0.904	2.312 (536)	0.0002
8 ^{2}A	2.467 (503)	0.006	0.545	2.529 (490)	nd
9 ^{2}A	2.527 (491)	0.001	0.894	2.889 (429)	0.0005
10 ^{2}A	2.621 (474)	0.001	0.562		

[a]Δ*E* in eV and (in parentheses) nm units. [b]Experimental values from the ref 22 electronic absorbance spectrum for Compound 1; nd = not determined.

mechanism.[44,45] However, the results were generally similar for both functionals. The bright state is well reproduced in the 5 ^{2}A state for all systems except for the Scheme 3 compound, where the bright state is 3 ^{2}A, and the difference in qCT is observed only in the highest excited states. Therefore, the discussion below is carried out with regard to B3-LYP functional results. For completeness, the results collected with the long-range functional are shown in Tables S8−S15.

From the oscillator strength values for the $SCPh_3$ complex reported in Table 1, the only bright state apparent is 5 ^{2}A, which as discussed below is the excited state in resonance with the incident radiation field in the RR process. The NTO of this state, depicted in Figure 1, shows considerable involvement of the S and Cu atoms in the transition. The amount of charge transfer, qCT, is above 0.5 *e* for all excited states (Table 1) indicating that all states have partial intramolecular charge transfer character between the three fragments.

The omega matrices are displayed in Figure 2 and indicate the extent of involvement of each fragment in the excitation. The horizontal and vertical axes plot the hole (occupied) and the electron (virtual) states, respectively. The blue color indicates regions of greatest charge transfer character. Diagonal elements (bottom left to top right) represent local excitations, while off-diagonal elements reflect properties of charge transfer states. From Figure 2, it follows that the first four excited states (1−4 ^{2}A) for the $SCPh_3$ complex are primarily localized on the Cu atom (Fragment 2), with some charge transfer from Cu into the thiolate ligand (Fragment 3). Furthermore, 1 ^{2}A and the bright state 5 ^{2}A (2.0 eV; 621 nm) show mixed charge transfer/excitonic characters in Fragments 2 and 3. Excited states 6 ^{2}A, 8 ^{2}A and 10 ^{2}A show mixed local excitations in the thiolate ligand (Fragment 3) with charge transfer into Cu (Fragment 2). These states also have approximately equal amounts of local excitation character in the thiolate group (Fragment 3). Finally, 7 ^{2}A and 9 ^{2}A are full charge transfer states (qCT ∼ 0.9 *e*).

Relative to the $SCPh_3$ complex, the excited state properties of Scheme 1 compounds that contain the *tert*-butyl ($SC(CH_3)_3$), *sec*-butyl ($SCH(CH_3)C_2H_5$) (all conformers A−D, Scheme 2), and pentafluorophenyl thiolate ($S(C_6F_5)$) thiolate ligands are similar (Tables S1−S6). The oscillator strength values suggest one bright state, 5 ^{2}A, with absorption energies in the 1.9−2.2 eV range and qCT just greater than 0.5 *e*. The omega matrices for the *tert*-butyl, *sec*-butyl, and pentafluorophenyl thiolate complexes are included in Figures S1−S6. The matrices are comparable for the *tert*-butyl and *sec*-butyl (all conformers, A−D) compounds, where like the $SCPh_3$

https://doi.org/10.1021/acssuschemeng.2c04802
ACS Sustainable Chem. Eng. 2022, 10, 14614−14623

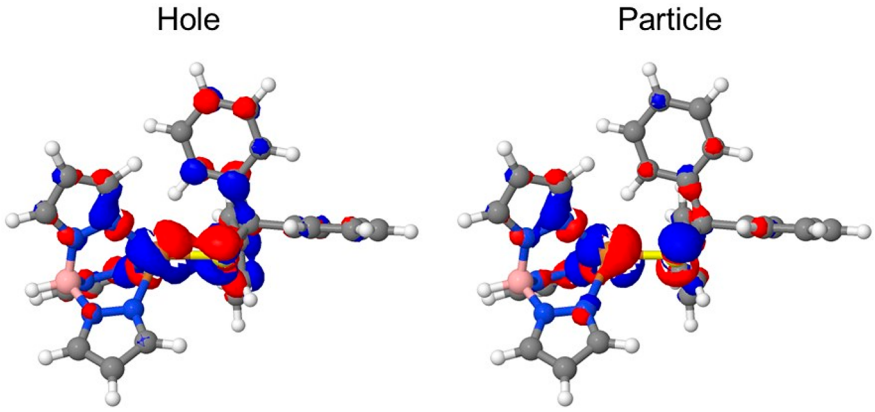

Figure 1. NTO for excited state 5 ^{2}A of the $SCPh_3$ complex (Scheme 1) in its ground state geometry using the B3-LYP-def2-TZVP approach. The iso-surface value was set at ±0.03 e/Bohr^3.

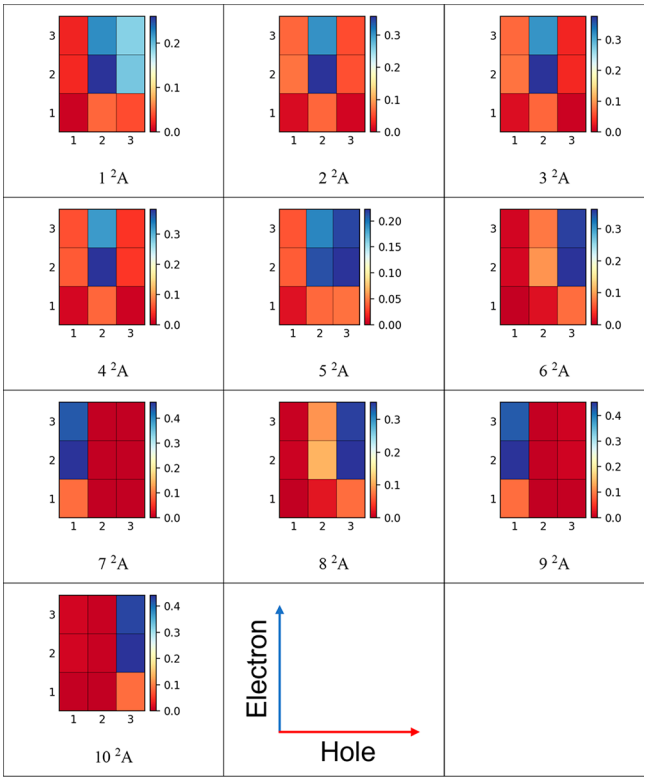

Figure 2. Omega matrices for excited states 1 ^{2}A−10 ^{2}A of the $SCPh_3$ complex in its ground state geometry calculated using the B3-LYP/def2-TZVP approach.

complex excited states 1−4 ^{2}A show strong local excitation in the Cu atom with significant charge transfer to the sulfur-containing fragment, while excited states 1 and 5 ^{2}A contain mixed charge transfer/excitonic characters in these fragments. The latter characteristics also are present in excited state 8 ^{2}A among the *tert*-butyl and *sec*-butyl complexes. For the S(C_6F_5) compound, most of the excited states can be described as above, but with differences in excited state 8 ^{2}A. The NTOs for the bright states of these Scheme 1 compounds are included in Figures S7−S8. Like the $SCPh_3$ complex (Figure 1), the hole density is "bonding" in character with respect to the Cu−S bond, while the particle density is "anti-bonding" showing a node between the two atoms. The characteristics reflect contributions of the highest occupied molecular orbital (HOMO) and the lowest occupied molecular orbital (LUMO) to the bright state (5 ^{2}A) NTO for each compound and have good consistency with an understanding developed through early in-depth studies of the $SCPh_3$ complex.[22] For completeness, the NTOs for the nine other excited states of the $SCPh_3$ complex calculated are included in Figures S9−S11.

Electronic Absorption Spectra. Resonance Raman spectra of blue copper proteins are excited by coupling into an intense electronic absorption band near 600 nm. Thus, it is of interest to simulate and inspect details of electronic absorption spectra before approaching the calculation of RR spectra. Figure 3 compares calculated and experimental

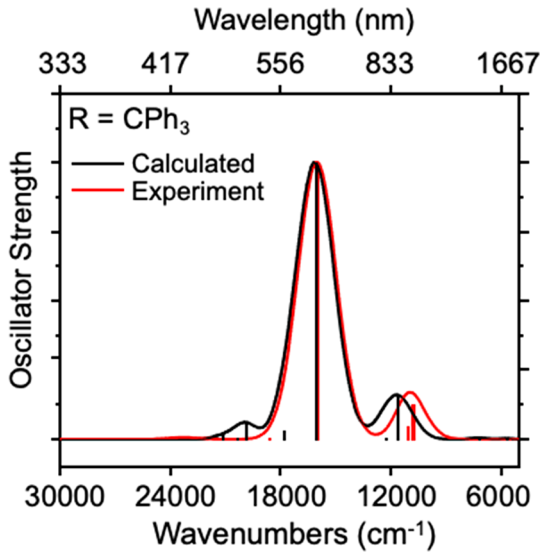

Figure 3. Calculated (black) and experimentally derived[22] (red) electronic absorption spectra of Scheme 1 compounds in which R = triphenylmethyl (CPh_3). Bars indicate the wavelength and relative oscillator strengths of the transitions. Solid lines show the resultant after convolution of the line spectra with a Gaussian band shape function (fwhm values are as reported in ref 22).

electronic absorption spectra of the $SCPh_3$ complex. The spectral energy range depicted encompasses transitions from the ground to the first 10 electronic excited states (Table 1). To facilitate the comparison, the spectra were normalized at the wavelength of maximum intensity. Although there are slight differences in the assignment of states (Table 1), the

https://doi.org/10.1021/acssuschemeng.2c04802
ACS Sustainable Chem. Eng. 2022, 10, 14614−14623

intensity variation across the spectrum is well predicted. The bright state was assigned to 6 ^{2}A in the experimental spectrum, while the calculations identify this state as 5 ^{2}A. Further, the second strongest transition was assigned to 4 ^{2}A in the experiment and 3 ^{2}A in the calculated spectrum. Despite these differences, the calculated and measured oscillator strengths for these two strong transitions are in good agreement. The minor discrepancies in the assignment of states may derive from the challenges associated with identifying the dark states in the experimental spectrum.

Figures S12 and S13 show calculated electronic absorption spectra for Scheme 1 compounds containing the *tert*-butyl, *sec*-butyl, or S(C_6F_5) thiolate ligands. Relative to the $SCPh_3$ complex, the calculated peak absorption shifts from 621 nm toward shorter wavelengths, into the 561−575 nm range, for the compounds substituted by $SC(CH_3)_3$ and $SCH(CH_3)$-C_2H_5 ligands. The shift is toward a longer wavelength, 659 nm, for the S(C_6F_5) complex. The peak absorption energies predicted for the $SCPh_3$ and S(C_6F_5) compounds are in excellent agreement with the experimental electronic absorption spectra of the synthesized compounds.[31] While the calculations overestimate the transition energy for the bright state of the *tert*-butyl and *sec*-butyl complexes by about 50 nm, the relative shifts of the peak maxima are consistent with the experiment and traceable to the electron withdrawing ability of the ligands.[31]

Resonance Raman spectra. *Simple Thiolate Complexes.* Figure 4 shows calculated normal and resonance Raman spectra of the $SCPh_3$ compound for excitations at 1200 and 621 nm, respectively, plotted on the scale of the absolute Raman scattering intensities.[46,47] The normal Raman spectrum is enlarged by a factor of 5 × 10^3 to enable the comparison. The strong enhancements that result from coupling into the 621 nm electronic excitation are evident, particularly through the low energy spectral region. Relative to the normal Raman spectrum, the peak intensities at 407 and 506 cm^{-1} are greater by more than 10^3. Inspecting the normal mode displacements for these bands indicates the 407 cm^{-1} vibration is dominated by Cu−S stretching, confirming the expectation of strong resonance Raman scattering from vibrational modes that have a considerable Cu−S stretching component upon excitation of the S pπ → Cu^{2+} charge transfer transition. The peak at 815 cm^{-1} in the resonance Raman spectrum traces to the first overtone of the Cu−S vibration. Since experimental RR spectra of the model T1 site mimics investigated have been limited to the region below 800 cm^{-1},[22,23,31] the computational results reported focus on this range.

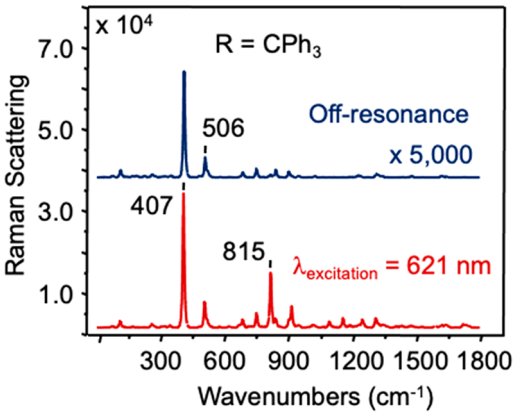

Figure 4. Simulated normal (top, blue) and resonance Raman (bottom, red) spectra from vertical excitation at 1200 and 621 nm, respectively, for the $SCPh_3$ compound (Scheme 1). The absolute Raman scattering intensities given in units of C^2 m^2 amu^{-1} V^2 are plotted.[43,44] The scale of the normal Raman spectrum is enlarged by 5 × 10^3 to enable comparison.

Figures 5 shows calculated resonance Raman spectra over this frequency region of practical interest.[22,23,31] The

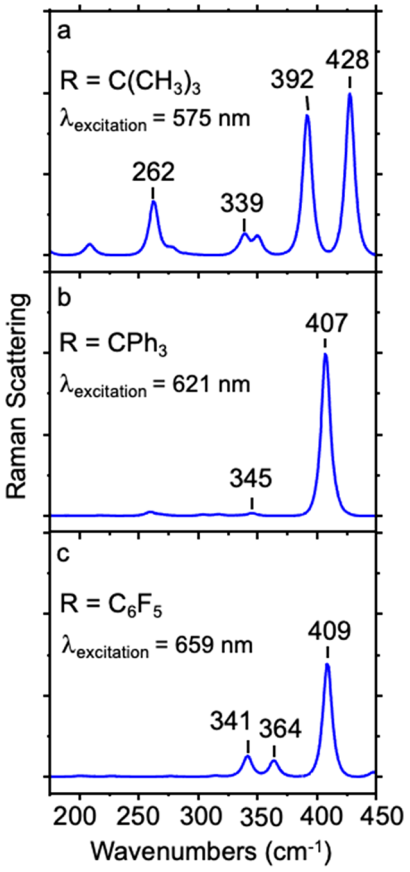

Figure 5. Simulated resonance Raman spectra over the region of the strong Cu−S stretching vibrational mode for Scheme 1 complexes containing the $SC(CH_3)_3$ (a), $SCPh_3$ (b), and S(C_6F_5) (c) ligands. For comparison, intensities are normalized to the strongest spectral bands in the range below 4000 cm^{-1} (428, 407, and 1380 cm^{-1}, for a, b, and c, respectively).

experimentally measured resonance Raman spectra for the compounds excited at 647 nm were dominated by a strong band near 420 cm^{-1} and contained weaker features toward lower energy. In each case, the peak near 420 cm^{-1} was assigned to a Cu−S stretching vibration, while the weaker bands were assigned to modes dominated by atomic displacements localized on the ligands.[31] Similarly, the calculated spectrum for each compound in Figure 5 predicts one transition assignable to a Cu−S stretching vibration and additional transitions that have atomic displacements localized on the ligands (Table 2).

To aid vibrational band assignments, in experimental studies, a resonance Raman spectrum of the complex containing the $SC(CH_3)_3$ thiolate ligand was recorded after replacement of all the *tert*-butyl protons with deuterium ($SC(CD_3)_3$). Taking a similar approach, Figure 6 compares the calculated resonance Raman spectra of the two complexes. From inspection of the

https://doi.org/10.1021/acssuschemeng.2c04802
ACS Sustainable Chem. Eng. 2022, 10, 14614−14623

Table 2. Observed and Calculated Frequencies (cm^{-1}) for Scheme 1 Complexes[a]

	SPh_3		$SC(CH_3)_3$		SC_6F_5	
Mode	Exp	Calc	Exp	Calc	Exp	Calc
Cu−S str.	422 *s*	407 *s*	437 *s*	428 *s*	409 *s*	409 *s*
t-butyl C−C−C[b]			400	392 *s*		
In-phase ligand[c]	324	345	348	339	354, 313	364, 341
Cu-pyrazole str.	233	190 *vw*	234	262	243	

[a]Experimental (Exp) values and mode assignments are from ref 31. Calc = calculated values; *s* and *vw* indicate strong and very weak resonance Raman scattering intensity, respectively. [b]C−C−C bending vibration[31] [c]Coupled, in-phase vibrational motion of the thiolate and pyrazole ligands.

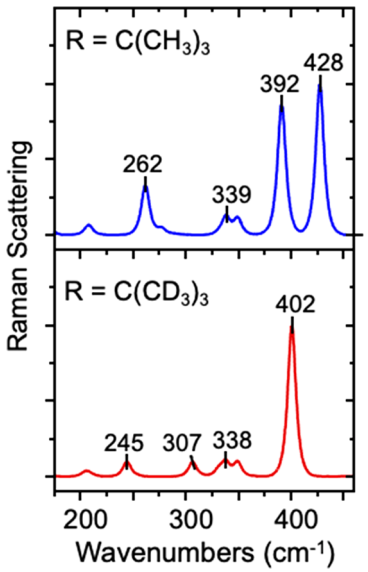

Figure 6. Simulated resonance Raman spectra over the region of the strong Cu−S stretching vibrational mode for the Scheme 1 complex containing the $SC(CH_3)_3$ (top) and $SC(CD_3)_3$ (bottom) ligands.

normal mode displacement coordinates, the 428 cm^{-1} band in Figure 5a for the complex containing the $SC(CH_3)_3$ ligand clearly maps to the Cu−S stretching vibrational mode. The vibration shifts to 402 cm^{-1}, a change of $\Delta\nu$ = −26 cm^{-1}, upon deuterium substitution (Figure 6). The shift to lower energy is consistent with the increased effective mass of the *tert*-butyl group. In measured spectra, a strong resonance Raman band assigned to the Cu−S stretching vibrational mode was observed at 437 cm^{-1} for the complex (Table 2). The band downshifted by $\Delta\nu$ = −26 to 411 cm^{-1} upon deuterium substitution, in close agreement with the calculated result.

The mode assignments and frequency shifts for the three additional bands indicated in Figure 6 also show good correspondence with the experiment (Table 3). The band at 392 cm^{-1} in Figure 6 (top) can be assigned to a vibrational mode consisting mainly of C−C−C bending within the $SC(CH_3)_3$ ligand[31] coupled to weak Cu−S stretching motion. Upon deuteration, the frequency downshifts to 338 cm^{-1} ($\Delta\nu$ = −54 cm^{-1}). Experimentally, the analogous features were observed at 400 and 340 cm^{-1} ($\Delta\nu$ = −60 cm^{-1}). The 339 cm^{-1} band (Figure 6, top) assigns to a vibrational mode composed of coupled, in-phase motions of the thiolate (C−C−S and C−C−C bending) and pyrazole (Cu−N stretching) groups, while the weak transition at 262 cm^{-1} is associated with Cu−pyrazole stretching coupled with Cu−S stretching and C−C−S bending motions. The deuterium isotope shifts for these modes and the close relationship to the experimentally measured transition frequencies and isotope shifts can be gleaned from Table 3.

Table 3. Observed and Calculated Frequencies (cm^{-1}) and Deuterium Isotope Shifts ($\Delta\nu$, cm^{-1}) for the *t*-Butyl Thiolate Complex[a]

	$SC(CD_3)_3$			
Mode	Exp	$\Delta\nu$	Calc	$\Delta\nu$
Cu−S str.	411 *s*	26	402 *s*	26
t-butyl C−C−C	340	60	338	54
In-phase ligand	306	42	307	32
Cu-pyrazole str.	223	11	245	17

[a]Abbreviations same as Table 2.

Although the RR calculations provide reasonable estimates of vibrational frequencies for the $SC(CH_3)_3$ and $SC(CD_3)_3$ complexes, the predicted transition intensity of the ligand-centered vibrational mode at 392 cm^{-1} (Figures 5a and 6 (top)) is considerably stronger than expected. A related disparity is present in the calculated spectrum of the $SCPh_3$ compound (Figure 5b), although in this case the intensity (at 345 cm^{-1}) is weaker than observed in experimental RR spectra.[23,31] For the latter compound, the vibrational mode traces to coupled Cu−N and S−C stretching within the ligands surrounding the Cu−S bond. The intensity disparities calculated likely reflect the challenge of predicting the extent of charge displacement from the Cu−S bond to the surrounding ligands upon excitation of the electronic transition.

In general, the calculated band positions and deuterium substitution effects for the compounds containing $SC(CH_3)_3$ and $SCPh_3$ ligands (Figures 5 and 6) are in good agreement with experiment. The key resonance Raman bands for the $SCPh_3$ complex near 408 and 345 cm^{-1} map to the 428 and 339 cm^{-1} transitions calculated for the $SC(CH_3)_3$ compound. The 392 cm^{-1} band in spectra of the latter is unique to the $SC(CH_3)_3$ ligand.

Resonance Raman transitions calculated for the Cu^{2+} complex containing the SC_6F_5 ligand are depicted in Figure 5c. As anticipated, the 409 cm^{-1} band arises from a strong Cu−S stretching motion. The bands at 364 and 341 cm^{-1} are associated with in-phase motions of the thiolate and pyrazole ligands, mapping to the vibration near 340 cm^{-1} in the complexes containing $SCPh_3$ and $SC(CH_3)_3$ groups. The calculation contrasts the experimental result somewhat, where two weak bands observed near 340 and 306 cm^{-1} were assigned to ligand deformation modes.[31]

Among the ligand variations considered in Figure 5, the calculated results are consistent with important trends that have been observed experimentally. First, each complex is predicted to have one dominant Cu−S stretching vibrational mode with frequency near 420 cm^{-1}. In addition, each

https://doi.org/10.1021/acssuschemeng.2c04802
ACS Sustainable Chem. Eng. 2022, 10, 14614−14623

compound has a vibration near 340 cm^{-1} that originates with in-phase motions of the pyrazole and thiolate ligands. Finally, the peak scattering intensity associated with the dominant Cu−S stretching vibrational mode is sensitive to the nature of the thiolate ligand. The vibration shifts to lower frequencies according to $SC(CH_3)_3$ > $SCPh_3$ > SC_6F_5 in experimental RR spectra, a trend ascribed to ligand electron withdrawing effects.[31] The slightly different trend in the calculated spectra ($SC(CH_3)_3$ > $SCPh_3$ ≈ SC_6F_5) derives from underestimation of the vibrational mode frequency by 10−15 cm^{-1} for compounds containing the $SC(CH_3)_3$ and $SCPh_3$ ligands.

Scheme 1 Complex Containing the sec-Butyl Thiolate Ligand. Results of RR calculations on the Scheme 1 complex containing the *sec*-butyl thiolate ligand are summarized in Figure 7 and Table S16. In early studies, the ligand added the

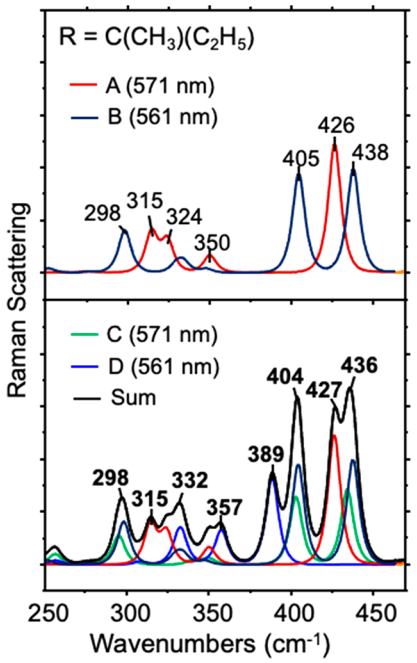

Figure 7. Simulated resonance Raman spectra comparing responses for the Scheme 1 complex containing the *sec*-butyl thiolate ligand in the conformations indicated. The inset includes the vertical excitation frequencies. The absolute scattering intensities are plotted.

complexity needed to advance understanding of the structure of the Cu^{2+} center at the enzymatic T1 active site.[31] In experimental studies, RR spectra of the *sec*-butyl thiolate complex excited at 647 nm were dominated by three intense bands at 446, 432, and 412 cm^{-1}.[31] A normal coordinate analysis attributed the three bands to vibrational modes that contain a Cu−S stretching component and showed sensitivity to conformation about the thiolate ligand S−C bond.[31] Consistent with this earlier work, the spectra in Figure 7 predict multiple intense bands between 400 and 450 cm^{-1} and reinforce the importance of considering contributions from different possible conformations.

Particularly relevant to the enzyme system is the staggered conformation that places the ethyl group trans to the Cu atom (Scheme 2A). The conformation is attained at the global minimum energy for the complex. The RR calculation predicts one dominant Cu−S stretching transition near 426 cm^{-1} (Figure 7, top), similar to the complex containing the *tert*-butyl ligand. However, in the *sec*-butyl complex, the Cu−S stretching coordinate is more strongly coupled to bending coordinates within the thiolate ligand, with almost exclusive mixing into the ethyl group S−C1−C3 bending coordinate for the Scheme 2A structure. Rotating slightly to the stable conformation that places the Cu and H in an eclipsed orientation (Scheme 2B) gives rise to two strong Cu−S stretching transitions, one just above and the other below 426 cm^{-1} (Figure 7, top). These can be mapped to the experimentally observed 446 and 412 cm^{-1} bands that trace to the respective ν_1 and ν_3 modes assigned from the earlier normal coordinate analysis of the conformation.[31] When the structure is rotated further to the staggered form that places the methyl group trans to the Cu atom (Scheme 2C), the calculated RR spectrum is nearly unchanged from that of the B conformation in Figure 7. To enable the potential contribution of each conformation to a composite spectrum to be compared in Figure 7, the absolute rather than the relative transition intensities are plotted.

The Scheme 2A−C structures were the focus of detailed normal coordinate analysis calculations by Spiro and co-workers.[31] For completeness, we examined the remaining staggered conformation (Scheme 2D). As anticipated, the Scheme 2D conformation is not predicted to display strong RR transitions in the 400−500 cm^{-1} range. The mode with the greatest Cu−S stretching component is associated with the transition near 389 cm^{-1}.

Our calculations indicate the barrier to free rotation about the S−C1 bond within the *sec*-butyl complex is small, below 1 kcal/mol. Thus, the experimental RR spectra (measured at 77 K)[31] likely reflect effects of the stable conformers in Scheme 2A−D. The composite spectrum in Figure 7 (bottom) shows the features that result when these component spectra are summed. The pattern of peaks linked to Cu−S stretching transitions above 400 cm^{-1} and the weaker transition near 389 cm^{-1} from the Figure 7D structure reproduce the trend observed in the experimental RR spectrum.[31]

Scrutinizing the calculated RR transitions further, the responses can be traced to effects of the dihedral angle that connects the Cu−S and C1−C3−C4 bonds. When the angle is 180° (Scheme 2A), the Cu−S stretching coordinate couples strongly with the in-plane S−C1−C3 angle bending coordinate. For the eclipsed structure (Scheme 2B), in contrast, the Cu−S stretching motion is coupled into both the ethyl and methyl groups through the C−C−C bending coordinates. The separation of bands in the eclipsed structure can be understood by considering the local symmetry within the thiolate ligand and its influence on the C−C−C motions. Unlike the *tert*-butyl group, the *sec*-butyl thiolate ligand lacks local 3-fold symmetry about the C−S bond axis.[31] As a result, the eclipsed structure contains two different C−C−C bending coordinates, one centered on C1−C3−C4 within the ethyl group and the other involving atoms of both the methyl and ethyl groups (C2−C1−C3). Indeed, the vibrational coordinate displacements show the calculated 438 cm^{-1} RR transition couples the Cu−S stretching with S−C stretching and the C2−C1−C3 bending coordinates, while the 405 cm^{-1} RR transition couples the Cu−S stretching with slightly more localized ethyl group atomic motions through the C1−C3−C4 bending coordinate. Similarly, for the eclipsed structure, the normal coordinate analysis of Spiro and co-workers predicted two strong Cu−S stretching transitions at frequencies associated with the experimentally observed RR bands at 446 and 412 cm^{-1}. A mode at intermediate frequencies for the structure

https://doi.org/10.1021/acssuschemeng.2c04802
ACS Sustainable Chem. Eng. 2022, 10, 14614−14623

lacked a Cu−S stretching component and was expected to be inactive under conditions of the RR spectra recorded.[31]

At lower frequencies, transitions near 290−360 cm^{-1} are associated with vibrational modes that couple pyrazole ligand Cu−N stretching and thiolate group displacements. For example, like the *tert*-butyl complex weak transitions at 350 and 330 cm^{-1} for the respective Scheme 2A and D conformations of the *sec*-butyl complex map to a mode that couples thiolate C−C−C bending with Cu−N stretching. The analogous feature in the experimental spectrum is likely the intermediate 332 cm^{-1} band, which also is prominent in the calculated composite spectrum of Figure 7 (bottom). Although it was not possible to record experimental spectra below about 320 cm^{-1}, the calculations indicate the possibility of observing significant low energy features. In Figure 7, the transitions near 315 and 298 cm^{-1} for the respective A and B conformations arise from weak coupling of Cu−S stretching into the HC−CH torsion coordinate unique to the *sec*-butyl ligand.

Laccase Enzymatic T1 Site Models. In the study of laccase enzymes, understanding derived from RR spectra of early Scheme 1 compounds was applied to a T1 site mimic depicted in Scheme 3. Typical of the T1 center in fungal laccases, the *β*-diketiminate compound ($L_2CuSCPh_3$) has three strong ligand interactions that stabilize the Cu^{2+} atom.[23] The compound is structurally related to those in Scheme 1 but has three instead of four Cu^{2+}−ligand bonds. Similar to the Scheme 1 complexes, the calculated electronic absorbance spectrum for the $L_2CuSCPh_3$ compound (Figure S14 and Table S7) is in good agreement with the experiment. The bright state is 3 ^{2}A with excitation energy near 1.7 eV (729 nm), which is lower than the bright state energies of the other compounds investigated (Tables S1−S6), consistent with the lower frequencies used experimentally[23] for excitation of $L_2CuSCPh_3$ RR spectra (752 nm). The omega matrix for the complex (Figure S15) shows the Cu (Fragment 2) and thiolate (Fragment 3) moieties play dominant roles in the charge transfer. In the bright state (3 ^{2}A), charge transfer from the thiolate to the Cu fragment occurs along with local excitation in the thiolate (Fragment 3). In contrast to those in Scheme 1, the $L_2CuSCPh_3$ complex lacks excited states with large values (>0.7 *e*) of qCT and displays more excitonic charge transfer character (qCT = 0.2 *e*) in excited state 10 ^{2}A. The NTOs for the bright state (Figure S16) have charge transfer characters similar to those of the Scheme 1 compounds (Figure 1 and Figures S7 and S8), but with somewhat less hole density in the region of the Cu−S bond. The more localized distribution of charge in the hole state for the $L_2CuSCPh_3$ compound likely reflects the fewer Cu−N ligation interactions relative to the Scheme 1 compounds.

The ORCA simulated RR spectrum for $L_2CuSCPh_3$ excited at the calculated vertical transition energy of 730 nm is shown in Figure 8. The transition energies are summarized in Table S17. The main features of the experimental spectrum are reproduced, with one strong band at 411 cm^{-1} traceable to the Cu−S stretching motion and weaker transitions toward lower frequency associated with ligand vibrations. The strong band in the experimental spectrum appears at 428 cm^{-1}.[23] The displacement vectors for the 366 cm^{-1} transition in Figure 8 indicate the vibrational mode consists of coupled Cu−N and Cu−S stretching motions, analogous to the transition calculated for the $SCPh_3$ complex at 345 cm^{-1} (Figure 5b) and the assignment for the 370 cm^{-1} band in the experimental spectrum. Two very weak bands at 321 and 303 cm^{-1} in Figure 8 have counterparts at 333 and 297 cm^{-1} in the experimental spectrum.[23] The vibrational modes for these transitions as well as those at 260 and 217 cm^{-1} involve motion of atoms throughout the *β*-diketiminate ligands and are unique to the $L_2CuSCPh_3$ compound.

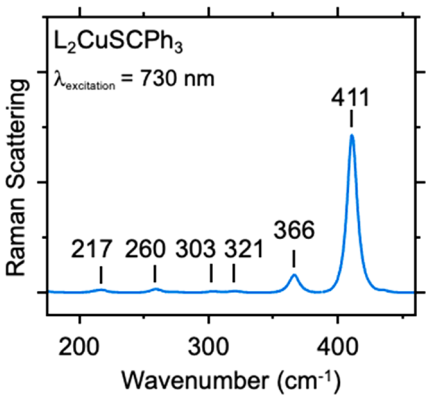

Figure 8. Simulated resonance Raman spectrum plotted over the region of the strong Cu−S stretching vibrational mode for the Scheme 3 small molecule ($L_2CuSCPh_3$) fungal laccase mimic.

Calculations on $L_2CuSCPh_3$ and Scheme 1 complexes form a foundation for approaching the analysis of laccase enzyme RR spectra. Ongoing efforts are examining a fungal laccase for which structure at the T1 site has been explored through mutations in residues coordinating the Cu atoms.[21] Computational models are being constructed from atomic structural data available in the Protein Data Bank.[48] A long-range goal of continued modeling and experimental RR studies targets the bacterially expressed laccase, small laccase (SLAC) of *Streptomyces coelicolor*, for its importance in the development of biofuel cell cathodes and its ease of isolation and purification for *in situ* Raman measurements.[15,49,50]

CONCLUSIONS

The TDDFT simulations performed produce electronic absorption and RR spectra that are in good agreement with experimentally measured spectra of the model Cu^{2+} complexes studied. The calculated electronic transition energies and oscillator strengths predict the strong absorption observed near 600 nm for the tris(pyrazolyl)hydroborate compounds and the downshift toward 740 nm for the lower coordination *β*-diketiminate complex. The NTOs of the bright states for the compounds indicate that a change from bonding to antibonding character occurs in the region of the Cu−S bond during the hole-to-particle transition, reflecting contributions of the HOMO/LUMO levels to the bright state. Consistent with these changes in electronic structure, the calculated RR spectra are dominated by a strong transition near 400 cm^{-1} traceable to a Cu−S stretching vibrational mode. An analysis of stable isomers of the *sec*-butyl thiolate complex (Scheme 2) confirms the sensitivity of the low energy spectral region to subtle variations in ligand geometry[31] and the need to consider atomic structure within the extended ligand sphere in interpretating RR spectra of blue copper proteins.[21,31] Building from the reported work, the TDDFT approach is being applied to explore relationships between measured RR spectra and ligand structures at the Cu^{2+} centers of well-characterized blue copper proteins and the SLAC enzyme relevant to biofuel cell development. The close match between theory and experiment demonstrated in the reported

https://doi.org/10.1021/acssuschemeng.2c04802
ACS Sustainable Chem. Eng. 2022, 10, 14614−14623

work provides a path for greater application of TDDFT in the study of electronic properties and RR spectra of many molecular complexes important in the advancement of sustainable chemistry.

■ ASSOCIATED CONTENT

Supporting Information

The Supporting Information is available free of charge at https://pubs.acs.org/doi/10.1021/acssuschemeng.2c04802.

Schemes 1−3. Tables of vertical excitation energy, oscillator strength, and charge transfer values for compounds computed with the B3-LYP and ωB97X-D3 functionals. Tables of transition frequencies and assignments for Schemes 2 and 3 compounds. Omega matrices and bright state natural transition orbitals (NTOs) for all compounds. NTOs for the excited states of Scheme 1 $SCPh_3$ complex. Table of optimized geometries. (PDF)

■ AUTHOR INFORMATION

Corresponding Authors

Adelia J. A. Aquino − *Department of Mechanical Engineering, Texas Tech University, Lubbock, Texas 79409, United States*; Email: adelia.aquino@ttu.edu

Carol Korzeniewski − *Department of Chemistry and Biochemistry, Texas Tech University, Lubbock, Texas 79409-1061, United States*; orcid.org/0000-0003-3672-0731; Email: carol.korzeniewski@ttu.edu

Authors

Umut Ozuguzel − *Department of Chemistry and Biochemistry, Texas Tech University, Lubbock, Texas 79409-1061, United States*; orcid.org/0000-0003-4891-6512

Reed Nieman − *Department of Chemistry and Biochemistry, Texas Tech University, Lubbock, Texas 79409-1061, United States*; orcid.org/0000-0003-3011-5223

Shelley D. Minteer − *Department of Chemistry, University of Utah, Salt City, Utah 84112, United States*; orcid.org/0000-0002-5788-2249

Complete contact information is available at: https://pubs.acs.org/10.1021/acssuschemeng.2c04802

Notes

The authors declare no competing financial interest.

■ ACKNOWLEDGMENTS

We gratefully acknowledge financial support from the U.S. National Science Foundation (NSF) through Grants CBET-1922956 (C.K.) and CBET-1921075 (S.D.M.) and allocations of computer time from the Texas Tech University High Performance Computing Center (HPCC).

■ REFERENCES

(1) Yang, Y.; Peltier, C. R.; Zeng, R.; Schimmenti, R.; Li, Q.; Huang, X.; Yan, Z.; Potsi, G.; Selhorst, R.; Lu, X.; Xu, W.; Tader, M.; Soudackov, A. V.; Zhang, H.; Krumov, M.; Murray, E.; Xu, P.; Hitt, J.; Xu, L.; Ko, H.-Y.; Ernst, B. G.; Bundschu, C.; Luo, A.; Markovich, D.; Hu, M.; He, C.; Wang, H.; Fang, J.; DiStasio, R. A., Jr.; Kourkoutis, L. F.; Singer, A.; Noonan, K. J. T.; Xiao, L.; Zhuang, L.; Pivovar, B. S.; Zelenay, P.; Herrero, E.; Feliu, J. M.; Suntivich, J.; Giannelis, E. P.; Hammes-Schiffer, S.; Arias, T.; Mavrikakis, M.; Mallouk, T. E.; Brock, J. D.; Muller, D. A.; DiSalvo, F. J.; Coates, G. W.; Abruña, H. D. Electrocatalysis in alkaline media and alkaline membrane-based energy technologies. *Chem. Rev.* **2022**, *122*, 6117−6321.

(2) Li, H.; Zeng, R.; Feng, X.; Wang, H.; Xu, W.; Lu, X.; Xie, Z.; Abruña, H. Oxidative stability matters: A case study of palladium hydride nanosheets for alkaline fuel cells. *J. Am. Chem. Soc.* **2022**, *144*, 8106−8114.

(3) Yang, Y.; Chen, G. Y.; Zeng, R.; Villarino, A. M.; DiSalvo, F. J.; van Dover, R. B.; Abruña, H. D. Combinatorial studies of palladium-based oxygen reduction electrocatalysts for alkaline fuel cells. *J. Am. Chem. Soc.* **2020**, *142*, 3980−3988.

(4) Li, Z.; Yang, Y.; Yin, Z.; Wei, X.; Peng, H.; Lyu, K.; Wei, F.; Xiao, L.; Wang, G.; Abruña, H. D.; Lu, J.; Zhuang, L. Interface-enhanced catalytic selectivity on the C_2 products of CO_2 electroreduction. *ACS Catal.* **2021**, *11*, 2473−2482.

(5) Chen, H.; Simoska, O.; Lim, K.; Grattieri, M.; Yuan, M.; Dong, F.; Lee, Y. S.; Beaver, K.; Weliwatte, S.; Gaffney, E. M.; Minteer, S. D. Fundamentals, applications, and future directions of bioelectrocatalysis. *Chem. Rev.* **2020**, *120*, 12903−12993.

(6) Mano, N.; de Poulpiquet, A. O_2 reduction in enzymatic biofuel cells. *Chem. Rev.* **2018**, *118*, 2392−2468.

(7) Milton, R. D.; Cai, R.; Abdellaoui, S.; Leech, D.; De Lacey, A. L.; Pita, M.; Minteer, S. D. Bioelectrochemical Haber-Bosch Process: An Ammonia-Producing H_2/N_2 Fuel Cell. *Angew. Chem., Int. Ed.* **2017**, *56*, 2680−2683.

(8) Khadka, N.; Milton, R. D.; Shaw, S.; Lukoyanov, D.; Dean, D. R.; Minteer, S. D.; Raugei, S.; Hoffman, B. M.; Seefeldt, L. C. Mechanism of Nitrogenase H_2 Formation by Metal-Hydride Protonation Probed by Mediated Electrocatalysis and H/D Isotope Effects. *J. Am. Chem. Soc.* **2017**, *139*, 13518−13524.

(9) Foster, S. L.; Bakovic, S. I. P.; Duda, R. D.; Maheshwari, S.; Milton, R. D.; Minteer, S. D.; Janik, M. J.; Renner, J. N.; Greenlee, L. F. Catalysis for nitrogen reduction to ammonia. *Nat. Catal.* **2018**, *1*, 490−500.

(10) Yuan, M.; Sahin, S.; Cai, R.; Abdellaoui, S.; Hickey, D. P.; Minteer, S. D.; Milton, R. D. Creating a low-potential redox polymer for efficient electroenzymatic CO_2 reduction. *Angew. Chem., Int. Ed.* **2018**, *57*, 6582−6586.

(11) Cai, R.; Milton, R. D.; Abdellaoui, S.; Park, T.; Patel, J.; Alkotaini, B.; Minteer, S. D. Electroenzymatic C-C bond formation from CO_2. *J. Am. Chem. Soc.* **2018**, *140*, 5041−5044.

(12) Mateljak, I.; Monza, E.; Lucas, M. F.; Guallar, V.; Aleksejeva, O.; Ludwig, R.; Leech, D.; Shleev, S.; Alcalde, M. Increasing Redox Potential, Redox Mediator Activity, and Stability in a Fungal Laccase by Computer-Guided Mutagenesis and Directed Evolution. *ACS Catal.* **2019**, *9*, 4561−4572.

(13) Ó Conghaile, P.; Falk, M.; MacAodha, D.; Yakovleva, M. E.; Gonaus, C.; Peterbauer, C. K.; Gorton, L.; Shleev, S.; Leech, D. Fully Enzymatic Membraneless Glucose|Oxygen Fuel Cell That Provides 0.275 mA cm−2 in 5 mM Glucose, Operates in Human Physiological Solutions, and Powers Transmission of Sensing Data. *Anal. Chem.* **2016**, *88*, 2156−2163.

(14) Scheiblbrandner, S.; Breslmayr, E.; Csarman, F.; Paukner, R.; Führer, J.; Herzog, P. L.; Shleev, S. V.; Osipov, E. M.; Tikhonova, T. V.; Popov, V. O.; Haltrich, D.; Ludwig, R.; Kittl, R. Evolving stability and pH-dependent activity of the high redox potential Botrytis aclada laccase for enzymatic fuel cells. *Sci. Rep.* **2017**, *7*, 13688.

(15) Gallaway, J.; Wheeldon, I.; Rincon, R.; Atanassov, P.; Banta, S.; Barton, S. C. Oxygen-reducing enzyme cathodes produced from SLAC, a small laccase from *Streptomyces coelicolor*. *Biosens. Bioelectron.* **2008**, *23*, 1229−1235.

(16) Wheeldon, I. R.; Gallaway, J. W.; Barton, S. C.; Banta, S. Bioelectrocatalytic hydrogels from electronconducting metallopolypeptides coassembled with bifunctional enzymatic building blocks. *P. Natl. Acad. Sci. USA* **2008**, *105*, 15275−15280.

(17) Shleev, S.; Tkac, J.; Christenson, A.; Ruzgas, T.; Yaropolov, A. I.; Whittaker, J. W.; Gorton, L. Direct electron transfer between copper-containing proteins and electrodes. *Biosens Bioelectron* **2005**, *20*, 2517−2554.

(18) Giroud, F.; Milton, R. D.; Tan, B.-X.; Minteer, S. D. Simplifying Enzymatic Biofuel Cells: Immobilized Naphthoquinone as a Biocathodic Orientational Moiety and Bioanodic Electron Mediator. *ACS Catal.* **2015**, *5*, 1240−1244.
(19) Jones, S. M.; Solomon, E. I. Electron transfer and reaction mechanism of laccases. *Cell. Mol. Life Sci.* **2015**, *72*, 869−883.
(20) Cai, R.; Abdellaoui, S.; Kitt, J. P.; Irvine, C.; Harris, J. M.; Minteer, S. D.; Korzeniewski, C. Confocal Raman Microscopy for the Determination of Protein and Quaternary Ammonium Ion Loadings in Biocatalytic Membranes for Electrochemical Energy Conversion and Storage. *Anal. Chem.* **2017**, *89*, 13290−13298.
(21) Augustine, A. J.; Kragh, M. E.; Sarangi, R.; Fujii, S.; Liboiron, B. D.; Stoj, C. S.; Kosman, D. J.; Hodgson, K. O.; Hedman, B.; Solomon, E. I. Spectroscopic Studies of Perturbed T1 Cu Sites in the Multicopper Oxidases Saccharomyces cerevisiae Fet3p and Rhus vernicifera Laccase: Allosteric Coupling between the T1 and Trinuclear Cu Sites. *Biochemistry* **2008**, *47*, 2036−2045.
(22) Randall, D. W.; George, S. D.; Hedman, B.; Hodgson, K. O.; Fujisawa, K.; Solomon, E. I. Spectroscopic and Electronic Structural Studies of Blue Copper Model Complexes. 1. Perturbation of the Thiolate−Cu Bond. *J. Am. Chem. Soc.* **2000**, *122*, 11620−11631.
(23) Randall, D. W.; George, S. D.; Holland, P. L.; Hedman, B.; Hodgson, K. O.; Tolman, W. B.; Solomon, E. I. Spectroscopic and Electronic Structural Studies of Blue Copper Model Complexes. 2. Comparison of Three- and Four-Coordinate Cu(II)−Thiolate Complexes and Fungal Laccase. *J. Am. Chem. Soc.* **2000**, *122*, 11632−11648.
(24) Dong, S.; Ybe, J. A.; Hecht, M. H.; Spiro, T. G. H-bonding maintains the active site of Type 1 copper proteins: Site-directed mutagenesis of Asn38 in Poplar plastocyanin. *Biochemistry* **1999**, *38*, 3379−3385.
(25) Dong, S.; Spiro, T. G. Ground- and excited-state mapping of plastocyanin from resonance Raman spectra of isotope-laabeled proteins. *J. Am. Chem. Soc.* **1998**, *120*, 10434−10440.
(26) Qiu, D.; Dong, S.; Ybe, J.; Hecht, M.; Spiro, T. G. Variations in the Type I copper protein coordination group. Resonance Raman spectrum of ^{34}S-, ^{65}Cu-, and ^{15}N-labeled plastocyanin. *J. Am. Chem. Soc.* **1995**, *117*, 6443−6446.
(27) Andrew, C. R.; Yeom, H.; Valentine, J. S.; Karlsson, B. G.; van Pouderoyen, G.; Canters, G. W.; Loehr, T. M.; Sanders-Loehr, J.; Bonander, N. Raman Spectroscopy as an Indicator of Cu-S Bond Length in Type 1 and Type 2 Copper Cysteinate Proteins. *J. Am. Chem. Soc.* **1994**, *116*, 11489−11498.
(28) Dave, B. C.; Germanas, J. P.; Czernuszewicz, R. S. The first direct evidence for copper(II)-cysteine vibrations in blue copper proteins: Resonance Raman spectra of ^{34}S-Cys-labeled azurins reveal correlation of ccopper-sulfur stretching frequency with metal site geometry. *J. Am. Chem. Soc.* **1993**, *115*, 12175−12176.
(29) Siiman, O.; Young, N. M.; Carey, P. R. Resonance Raman spectra of "blue" copper proteins and the nature of their copper sites. *J. Am. Chem. Soc.* **1976**, *98*, 744−748.
(30) Nestor, L.; Larrabee, J. A.; Woolery, G.; Reinhammar, B.; Spiro, T. G. Resonance Raman spectra of blue copper proteins: assignments from normal mode calculations and copper-63/copper-65 and H2O/D2O shifts for stellacyanin and laccase. *Biochemistry* **1984**, *23*, 1084−1093.
(31) Qiu, D.; Kilpatrick, L.; Kitajima, N.; Spiro, T. G. Modeling blue copper protein resonance Raman spectra with thiolate-CuII complexes of a sterically hindered tris(pyrazolyl)borate. *J. Am. Chem. Soc.* **1994**, *116*, 2585−2590.
(32) Urushiyama, A.; Tobari, J. Resonance Raman Active Vibrations of Blue Copper Proteins. Normal Coordinate Analysis on 169-Atom Model. *Bull. Chem. Soc. Jpn.* **1990**, *63*, 1563−1571.
(33) Kitajima, N.; Fujisawa, K.; Morooka, Y. Tetrahedral copper(II) complexes supported by a hindered pyrazolylborate. Formation of the thiolato complex, which closely mimics the spectroscopic characteristics of blue copper proteins. *J. Am. Chem. Soc.* **1990**, *112*, 3210−3212.
(34) Neese, F.; Wennmohs, F.; Becker, U.; Riplinger, C. ORCA quantum chemistry program package. *J. Chem. Phys.* **2020**, *152*, 224108.
(35) Becke, A. D. Density-functional thermochemistry. III. The role of exact exchange. *J. Chem. Phys.* **1993**, *98*, 5648−5652.
(36) Hattig, C. Geometry Optimizations with the Coupled-Cluster Model CC2 Using the Resolution-of-the-Identity Approximation. *J. Chem. Phys.* **2003**, *118*, 7751−7761.
(37) Weigend, F.; Haser, M.; Patzelt, H.; Ahlrichs, R. RI-MP2: Optimized auxiliary basis sets and demonstration of efficiency. *Chem. Phys. Lett.* **1998**, *294*, 143−152.
(38) Schafer, A.; Horn, H.; Ahlrichs, R. Fully Optimized Contracted Gaussian-Basis Sets for Atoms Li to Kr. *J. Chem. Phys.* **1992**, *97*, 2571−2577.
(39) Plasser, F.; Lischka, H. Analysis of Excitonic and Charge Transfer Interactions from Quantum Chemical Calculations. *J. Chem. Theory Comput.* **2012**, *8*, 2777−2789.
(40) Martin, R. L. Natural transition orbitals. *J. Chem. Phys.* **2003**, *118*, 4775−4777.
(41) Plasser, F.; Wormit, M.; Dreuw, A. New Tools for the Systematic Analysis and Visualization of Electronic Excitations. I. Formalism. *J. Chem. Phys.* **2014**, *141*, 024106.
(42) Plasser, F. T. *TheoDORE: A Package for Theoretical Density, Orbital Relaxation, and Exciton Analysis*, 2021. http://theodore-qc.sourceforge.net (accessed October 2022).
(43) Lin, Y.-S.; Li, G.-D.; Mao, S.-P.; Chai, J.-D. Long-range corrected hybrid density functionals with improved dispersion corrections. *J. Chem. Theory Comput.* **2013**, *9*, 263−272.
(44) Dreuw, A.; Weisman, J. L.; Head-Gordon, M. Long-range charge-transfer excited states in time-dependent density functional theory require non-local exchange. *J. Chem. Phys.* **2003**, *119*, 2943−2946.
(45) Adamo, C.; Jacquemin, D. The calculations of excited-state properties with Time-Dependent Density Functional Theory. *Chem. Soc. Rev.* **2013**, *42*, 845−856.
(46) de Souza, B.; Farias, G.; Neese, F.; Izsák, R. Efficient simulation of overtones and combination bands in resonant Raman spectra. *J. Chem. Phys.* **2019**, *150*, 214102.
(47) Neugebauer, J.; Reiher, M.; Kind, C.; Hess, B. A. Quantum chemical calculation of vibrational spectra of large molecules - Raman and IR spectra for buckminsterfullerene. *J. Comput. Chem.* **2002**, *23*, 895−910.
(48) Burley, S. K; Berman, H. M; Bhikadiya, C.; Bi, C.; Chen, L.; Costanzo, L. D.; Christie, C.; Duarte, J. M; Dutta, S.; Feng, Z.; Ghosh, S.; Goodsell, D. S; Green, R. K.; Guranovic, V.; Guzenko, D.; Hudson, B. P; Liang, Y.; Lowe, R.; Peisach, E.; Periskova, I.; Randle, C.; Rose, A.; Sekharan, M.; Shao, C.; Tao, Y.-P.; Valasatava, Y.; Voigt, M.; Westbrook, J.; Young, J.; Zardecki, C.; Zhuravleva, M.; Kurisu, G.; Nakamura, H.; Kengaku, Y.; Cho, H.; Sato, J.; Kim, J. Y.; Ikegawa, Y.; Nakagawa, A.; Yamashita, R.; Kudou, T.; Bekker, G.-J.; Suzuki, H.; Iwata, T.; Yokochi, M.; Kobayashi, N.; Fujiwara, T.; Velankar, S.; Kleywegt, G. J; Anyango, S.; Armstrong, D. R; Berrisford, J. M; Conroy, M. J; Dana, J. M; Deshpande, M.; Gane, P.; Gaborova, R.; Gupta, D.; Gutmanas, A.; Koca, J.; Mak, L.; Mir, S.; Mukhopadhyay, A.; Nadzirin, N.; Nair, S.; Patwardhan, A.; Paysan-Lafosse, T.; Pravda, L.; Salih, O.; Sehnal, D.; Varadi, M.; Varekova, R.; Markley, J. L; Hoch, J. C; Romero, P. R; Baskaran, K.; Maziuk, D.; Ulrich, E. L; Wedell, J. R; Yao, H.; Livny, M.; Ioannidis, Y. E Protein Data Bank: the single global archive for 3D macromolecular structure data. *Nucleic Acids Res.* **2019**, *47*, D520−D528.
(49) Machczynski, M. C.; Vijgenboom, E.; Samyn, B.; Canters, G. W. Characterization of SLAC: A small laccase from *Streptomyces coelincolor* with unprecedented activity. *Protein Sci.* **2004**, *13*, 2388−2397.
(50) Dasgupta, R.; Gupta, K. B. S. S.; Nami, F.; de Groot, H. J. M.; Canters, G. W.; Groenen, E. J. J.; Ubbink, M. Chemical excchange at the trinuclear copper center of small laccase from *Streptomyces coelicolor*. *Biophys. J.* **2020**, *119*, 9−14.

https://doi.org/10.1021/acssuschemeng.2c04802
ACS Sustainable Chem. Eng. 2022, 10, 14614−14623